Dewatering of fibre suspensions by pressure filtration

Duncan R. Hewitt, Daniel T. Paterson, Neil J. Balmforth, and D. Mark Martinez

Articles you may be interested in

Size exclusion deep bed filtration: Experimental and modelling uncertainties
Rev. Sci. Instrum. **85**, 015111 (2014); 10.1063/1.4861096

Impact of tortuous flow on bacteria streamer development in microfluidic system during filtration
Biomicrofluidics **8**, 014105 (2014); 10.1063/1.4863724

Influence of microbial biofilms on reactive transport in porous media
AIP Conf. Proc. **1453**, 276 (2012); 10.1063/1.4711188

Filtration in electrorheological suspensions related to the Peclet number
J. Rheol. **54**, 591 (2010); 10.1122/1.3378762

Filtration of micron-sized particles in granular media revealed by x-ray computed tomography
Rev. Sci. Instrum. **76**, 103704 (2005); 10.1063/1.2103467

Dewatering of fibre suspensions by pressure filtration

Duncan R. Hewitt,[1,2] Daniel T. Paterson,[3] Neil J. Balmforth,[1]
and D. Mark Martinez[4]

[1]*Department of Mathematics, University of British Columbia, Vancouver,
British Columbia V6T 1Z2, Canada*
[2]*Department of Applied Mathematics and Theoretical Physics, University of Cambridge,
Cambridge, United Kingdom*
[3]*Department of Mechanical Engineering, University of British Columbia,
Vancouver, British Columbia V6T 1Z4, Canada*
[4]*Department of Chemical and Biological Engineering, University of British Columbia,
Vancouver, British Columbia V6T 1Z3, Canada*

A theoretical and experimental study of dewatering of fibre suspensions by uniaxial compression is presented. Solutions of a one-dimensional model are discussed and asymptotic limits of fast and slow compression are explored. Particular focus is given to relatively rapid compression and to the corresponding development of spatial variations in the solidity and velocity profiles of the suspension. The results of complementary laboratory experiments are presented for nylon or cellulose fibres suspended in viscous fluid. The constitutive relationships for each suspension were measured independently. Measurements of the load for different fixed compression speeds, together with some direct measurements of the velocity profiles using particle tracking velocimetry, are compared with model predictions. The comparison is reasonable for nylon, but poor for cellulose fibres. An extension to the model, which allows for a strain-rate-dependent component in the network stress, is proposed, and is found to give a dramatic improvement in the model predictions for cellulose fibre suspensions. The reason for this improvement is attributed to the microstructure of cellulose fibres, which, unlike nylon fibres, are themselves porous. *Published by AIP Publishing.* [http://dx.doi.org/10.1063/1.4952582]

I. INTRODUCTION

The removal of water from dense suspensions is an important process in a wide range of industrial settings including the consolidation of mine tailings and the treatment of waste-water and sludge.[6,21,27,31] In a more familiar household setting, it underpins the workings of a (French) coffee press. Related problems of consolidation and compaction feature in biological settings, including digestion in the gastrointestinal tract,[18] and in geophysics, notably in soil mechanics, sedimentary geology, and magma flow.[1,9] The primary motivation for the present work is the dewatering of cellulose fibre suspensions, which is essential to the papermaking process.[8]

More specifically, we present a combined theoretical and experimental study of dewatering under a fixed rate of compression. The dynamics of dewatering depends on the ratio of the compressive strength of the solid network to the viscous drag force exerted by the fluid on the solid as it flows out of the suspension, a dimensionless group that we denote by γ. We focus particularly on small values of γ, which corresponds to relatively rapid dewatering.

The process of dewatering can be described as a two-phase flow problem wherein a solid matrix is compressed, forcing the interstitial fluid phase to flow out of the medium. Models of dewatering are typically posed in one spatial dimension, with a suspension undergoing vertical compression by the application of a fixed load or fixed rate of compression, to form a compacted filter cake.[5,22,27] Modelling requires the introduction of constitutive laws to describe the effective stress that the solid network can support (the "compressive yield stress") and the permeability of the mixture to the flow of interstitial fluid. Both are functions of the local solid fraction ϕ. Indeed,

many previous studies have focussed on the development of experimental techniques to measure and calibrate these constitutive laws, without necessarily verifying the suitability of the two-phase flow model.[5,7,16]

We follow suit here and use a two-phase flow model, similar to works derived previously,[4,14,15] to underscore our theory. We present numerical solutions of the model and discuss its asymptotic limits for slow or fast compaction, focussing particularly on the formation of high-solid-fraction boundary layers below the piston in the limit of relatively rapid compression (small γ). However, rather than exploiting these as part of a calibration exercise for the permeability and compressive yield stress,[13] we determine these empirical functions independently, and then critically assess the model itself by comparison with a series of laboratory experiments.

The focus of these experiments is to investigate the dewatering of fibrous suspensions. Specifically, we used suspensions of cellulose and nylon fibres in a Newtonian fluid. The compressive yield stress and permeability of both were measured as functions of the solid fraction in specially designed load and permeability cells. Dewatering experiments were then performed at a range of different compression rates. Given the relatively low permeability and high compressive strength of the test materials, the experimental setup was designed to apply and sustain relatively large pressures. In some experiments, we also measured the local velocity profiles through the sample during the experiment by particle tracking velocimetry.

We find that the two-phase model gives good qualitative agreement with measurements from experiments with a nylon suspension. By contrast, the agreement is poor for cellulose fibre suspensions, with the model predicting qualitatively different behaviour from the experimental measurements under rapid compression. To improve this latter situation, we argue that the effective stress of the suspension is not given solely by the compressive yield stress, rather it also contains a viscous or rate-dependent component. While rheological expressions of this form have been suggested in previous work,[4,5] their effect on the behaviour of a dewatering suspension has not been explored. The inclusion of the more complex rheology into the model gives significantly better agreement with the experimental measurements for cellulose.

II. MATHEMATICAL FORMULATION

A. Governing equations

We consider a two-phase deformable medium or suspension comprising a solid and a fluid phase. The suspension fills a container with a rigid base and is compressed from above by a porous piston, which moves at a constant downwards speed U such that the piston is located at height $\hat{z} = \hat{h}(\hat{t}) = h_0 - U\hat{t}$, for some initial height h_0 (see Figure 1(a)). The corresponding load on the piston, which is not imposed, is denoted by $\sigma(t)$. As the solid phase is compressed, the fluid is assumed to pass freely through the porous piston with negligible resistance. The solid fraction or solidity ϕ of the suspension is initially larger than the "gel point" of the mixture, such that the solid phase can sustain compressive stress. In the subsequent analysis, we neglect gravity, inertia, and internal viscous stresses in the fluid phase, and we assume that the medium is constrained in the out-of-plane directions such that the deformation and motion remain one-dimensional. The individual constituent solid and fluid phases are each assumed to be incompressible, such that their density does not change. Under these assumptions, the equations of conservation of mass and momentum for one-dimensional flow in a two-phase medium can be written as

$$\frac{\partial \phi}{\partial \hat{t}} + \frac{\partial}{\partial \hat{z}}\left(\phi \hat{u}_s\right) = 0, \tag{1}$$

$$-\frac{\partial \phi}{\partial \hat{t}} + \frac{\partial}{\partial \hat{z}}\left[(1 - \phi)\,\hat{u}_f\right] = 0, \tag{2}$$

$$(1 - \phi)\left(\hat{u}_f - \hat{u}_s\right) = -\frac{k(\phi)}{\mu}\frac{\partial \hat{p}}{\partial \hat{z}}, \tag{3}$$

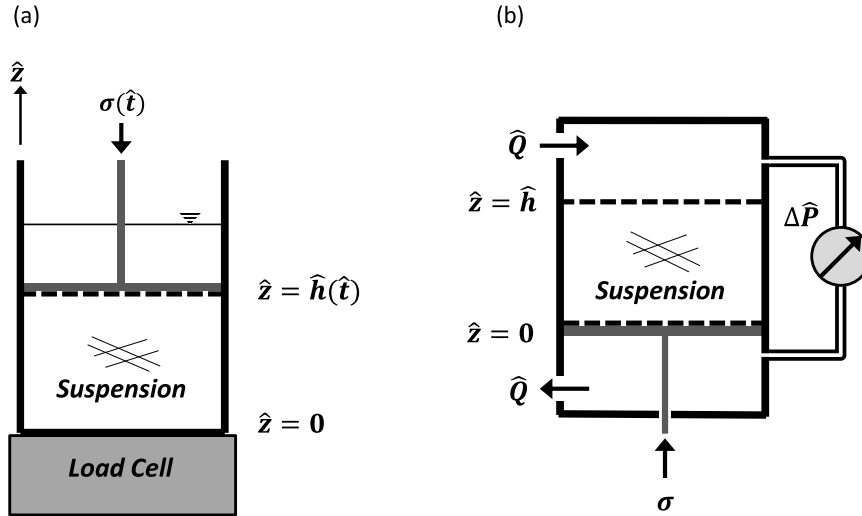$$\frac{\partial \hat{P}}{\partial \hat{z}} = 0, \tag{4}$$

FIG. 1. Schematic diagrams of (a) the dynamic dewatering device, which corresponds to the setup for the theoretical model, and (b) the permeability testing apparatus (see Sec. III).

where ϕ is the solidity or volume fraction of the solid phase, $\hat{u}_s$ and $\hat{u}_f$ refer to the velocities of the two phases, $k(\phi)$ is the permeability of the medium, μ is the viscosity, $\hat{p}$ is the pore pressure in the fluid phase, $\hat{P}$ is the bulk compressive stress on the two-phase mixture, and $\hat{z}$ and $\hat{t}$ denote vertical distance above the base of the container and time, respectively. Equations (1) and (2) describe conservation of mass in each phase, (3) is Darcy's law, and (4) indicates that the total stress is conserved. We note that an alternative and frequently used approach is to consider individual equations of momentum conservation[3] for each phase, coupled by a "momentum transfer" term. Given a suitable choice of transfer term, these equations can be rearranged to give (3) and (4); indeed, the form of the transfer term is difficult to predict and it is typically chosen so that Darcy's law is recovered after the rearrangement.

At the lower surface of the medium ($\hat{z} = 0$), no normal flow demands that $\hat{u}_f = \hat{u}_s = 0$, and so (1) and (2) can be combined and integrated to find

$$(1 - \phi)\hat{u}_f + \phi\hat{u}_s = 0 \qquad \text{or} \qquad (1 - \phi)(\hat{u}_s - \hat{u}_f) = \hat{u}_s. \tag{5}$$

Hence, from (3),

$$\hat{u}_s = \frac{k(\phi)}{\mu} \frac{\partial \hat{p}}{\partial \hat{z}}. \tag{6}$$

At the upper surface, the solid travels at the speed of the piston and the pore pressure vanishes, provided the piston offers no resistance to flow through it and the pressure of the overlying fluid is negligible. Thus $\hat{u}_s = -U$ and $\hat{p} = 0$ at $\hat{z} = \hat{h}(\hat{t})$. From (4), the applied load $\sigma(\hat{t})$ at the piston is conserved throughout the medium, such that $\hat{P} = \sigma(\hat{t})$.

Following Terzaghi's principle in soil mechanics, we define the effective solid stress or network stress $\mathcal{P}$ to be the overpressure on the solid network, given by

$$\mathcal{P} = \hat{P} - \hat{p} = \sigma(\hat{t}) - \hat{p}, \tag{7}$$

and we determine the form of $\mathcal{P}$ from a suitable constitutive model. The simplest and perhaps most widely used constitutive model for the network stress[1,3,15] uses

$$\mathcal{P} = p_y(\phi), \tag{8}$$

where the "compressive yield stress" p_y is a prescribed, increasing, function of the solid fraction. Thence, from (6),

$$\hat{u}_s = -\frac{k(\phi)p_y'(\phi)}{\mu} \frac{\partial \phi}{\partial \hat{z}}, \tag{9}$$

where $p'_y = \partial p_y / \partial \phi$. Equation (9) can be substituted into (1) to furnish a nonlinear diffusion equation for the solidity.

Previous authors have suggested or explored more involved constitutive laws than (8), to describe, for example, "plastic" evolution of the solidity when the stress exceeds the compressive yield stress,[4] or viscous compaction of the solid matrix.[20] We will consider an extension to the constitutive model when we discuss our experimental results in Section III E, but for the current outline of the model we retain the simple form in (8). Note that, in one spatial dimension, there is an explicit relationship between the solid fraction and the strain in the medium, and so a constitutive model of the form in (8) would also result from a simple poro-elastic rheology for the solid phase.[11]

B. Dimensionless model

We introduce dimensionless variables, denoted by the removal of the hat decoration, by scaling lengths by the initial depth h_0 of the medium and velocity by the speed U of the piston,

$$\hat{z} = h_0 z, \quad \hat{h} = h_0 h, \quad \hat{t} = \frac{h_0}{U} t, \quad \hat{u}_s(\hat{z}, \hat{t}) = U u(z, t). \tag{10}$$

If the permeability $k(\phi)$ and compressive yield stress $p_y(\phi)$ have characteristic dimensional scales k_* and p_*, respectively, we introduce dimensionless functions,

$$K(\phi) = \frac{k(\phi)}{k_*}, \quad \Pi_y(\phi) = \frac{p_y(\phi)}{p_*}, \quad \Sigma(t) = \frac{\sigma(\hat{t})}{p_*}, \tag{11}$$

and define the effective diffusivity,

$$D(\phi) = \frac{\phi k(\phi) p'_y(\phi)}{k_* p_*} \equiv \phi K(\phi) \Pi'_y(\phi). \tag{12}$$

Governing equations (1) and (9) combine to

$$\frac{\partial \phi}{\partial t} = -\frac{\partial}{\partial z}(u\phi) = \gamma \frac{\partial}{\partial z}\left[D(\phi)\frac{\partial \phi}{\partial z}\right], \tag{13}$$

where the dimensionless group

$$\gamma = \frac{p_* k_*}{\mu h_0 U} \tag{14}$$

is the ratio of the compressive strength of the solid to the viscous drag force from the fluid. Note that one can derive (13) by working with a "hindered-settling function" $R \sim (1-\phi)^2/(\phi k)$ rather than the permeability k, which gives an alternative, but equivalent, expression for the effective diffusivity D in terms of R.[17,27]

The boundary conditions are

$$u(0,t) = 0, \qquad u(h,t) = -1, \tag{15}$$

and

$$\Pi_y(\phi(h,t)) = \Sigma(t) \quad \text{at } z = h, \tag{16}$$

and the height is given by $h(t) = 1 - t$. At $t = 0$, the medium is well mixed so that $\phi(z,0) = \phi_0$, which is the initial solid fraction.

C. Solutions and analysis of the model

In principle, the model outlined above can be solved for any constitutive functions $k(\phi)$ and $p_y(\phi)$. Previous measurements of $p_y(\phi)$ and $k(\phi)$ for a variety of deformable media and suspensions show that, in general, p_y increases monotonically and k decreases monotonically as the solidity increases. A collection of our own and previous measurements of $k(\phi)$ and $p_y(\phi)$, and the diffusivity

$D(\phi)$ that they predict, will be discussed in Sec. III. In the following analysis, we adopt

$$K(\phi) = \frac{(1 - \phi)^a}{\phi^b}, \qquad \Pi_y(\phi) = \frac{\phi^n}{(1 - \phi)^m}, \tag{17}$$

with positive power-law exponents a, b, n, and m. Note that (17) assumes a maximum packing fraction of $\phi = 1$, where the permeability vanishes and the compressive stress diverges. Given (17), the effective diffusivity takes the transparent analytical form

$$D = [n + (m - n)\phi] \, \phi^{n-b}(1 - \phi)^{a-m-1}. \tag{18}$$

The trend of this diffusivity with ϕ depends on the choices for the exponents in the permeability and the compressive stress. Unless otherwise specified, the results in the following figures use default values of $a = 3$, $b = 2$, and $m = 2$ in (18), with different values of n to illustrate the effect of different diffusivity trends. In practice, we use $n = 1.5$ and $n = 3$ to illustrate the effect of a diffusivity that either decreases or increases with ϕ for small ϕ.

In Subsections II C 1 and II C 2, we discuss the asymptotic limits of slow or fast compaction, and compare asymptotic predictions with numerical solutions of (13). We solved (13) numerically using a standard second-order finite-difference discretization in space, with the substitution $y = z/h(t)$ to map the equation to a fixed domain and a semi-implicit time-stepping method.

1. Slow compaction: γ ≫ 1

The limit of slow compaction was discussed by Landman *et al.*[15] In brief, if $\gamma \gg 1$, to achieve a balance in (13), we must take $\partial\phi/\partial z = O(\gamma^{-1})$ as $u \sim O(1)$. Then,

$$\frac{\partial\phi}{\partial t} \sim -\phi\frac{\partial u}{\partial z} \qquad \text{or} \qquad \phi = \frac{\phi_0}{h} \qquad \text{and} \qquad u = -\frac{z}{h}, \tag{19}$$

given the boundary conditions in (15). In other words, ϕ is independent of z in this limit and the medium compacts uniformly. The force on the piston is $\Sigma(t) = \Pi_y(\phi_0/h)$, which is independent of the piston speed. From a practical point of view, the measured load therefore provides a direct measurement of the compressive stress $p_y(\phi)$ that is independent of any dynamics of the problem.

Figure 2(a) shows a series of measurements from sample solutions with $\gamma = 10^3$ and $n = 3$ (note that, since the diffusive term drops out of the equations in this limit, the precise value of n is insignificant in these examples). The solutions agree extremely well with the asymptotic predictions. Profiles for a lower value of γ (Figure 2(b)) show a small deviation from the quasi-static asymptotic solution at early times, with a slight accumulation of solid close to the piston.

2. Quick compaction: γ ≪ 1

A glance at (13) in the limit $\gamma \ll 1$ suggests that $u \sim 0$ and $\partial\phi/\partial t \sim 0$, with solution $\phi = \phi_0$, even after the initial moment. This solution fails to satisfy the top boundary condition, leading one to suspect that a boundary layer develops there, into which all the solid consolidates as the piston moves down. Provided $\phi \ll 1$, the boundary layer remains thin and accepts all the solid that is pushed into it.

To resolve the boundary layer, we transform into the frame of the upper surface and set $z = h(t) - \zeta$,

$$\frac{\partial\phi}{\partial t} - \frac{\partial\phi}{\partial\zeta} \sim \gamma\frac{\partial}{\partial\zeta}\left[D(\phi)\frac{\partial\phi}{\partial\zeta}\right]. \tag{20}$$

In the narrow boundary layer, $\zeta \ll h$ and the vertical derivatives become large, which in part counters the smallness of γ. The subsequent analysis can be couched in terms of formal asymptotics, which adds to the weight of the argument but requires a detailed consideration of the form of the diffusivity $D(\phi)$ in order to understand the precise scalings of the solution if $\phi_0 \ll 1$. We therefore avoid this formalization, which mostly involves confirming that $\partial\phi/\partial t$ in (20) can be neglected in comparison to the other two terms. Hence, in view of the top boundary condition,
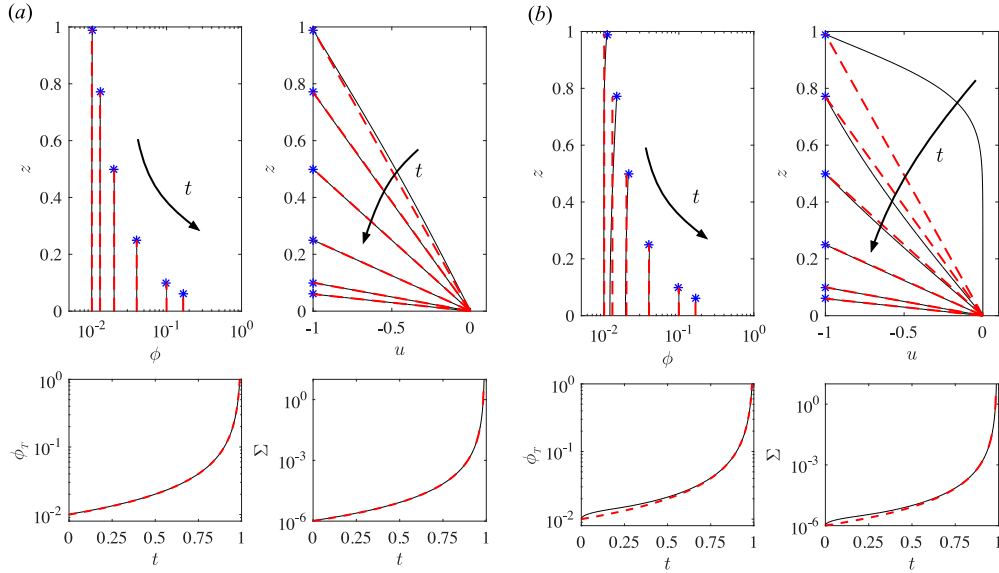
FIG. 2. Results for slow compaction ($\gamma \gg 1$). Numerical solutions (black solid lines) and leading-order asymptotic predictions for large γ from (19) (red dashed lines), for (a) $\gamma = 10^3$ and (b) $\gamma = 50$. Upper panels show a series of snapshots of the solid fraction $\phi(z)$ (top left) and solid speed $u(z)$ (top right) at different dimensionless times: $t = 0.01, 0.25, 0.5, 0.75, 0.9$, and 0.95. At each time, the blue star indicates the position of the piston. Lower panels show the solid fraction $\phi_T(t) \equiv \phi(z = h)$ at the piston (bottom left) and the corresponding load $\Sigma(t) = \Pi_y(\phi_T)$ on the piston (bottom right). All results have $n = 3$ and $\phi_0 = 0.01$.

$u = \gamma D \phi_\zeta / \phi = -1$ for $\zeta = 0$, the integral of (20) furnishes

$$-\phi = \gamma D \frac{\partial \phi}{\partial \zeta}. \tag{21}$$

Hence

$$F(\phi) = F(\phi_T) - \frac{\zeta}{\gamma}, \tag{22a}$$

$$F(\phi) \equiv \int D(\phi) \frac{\mathrm{d}\phi}{\phi}, \tag{22b}$$

$$\phi_T(t) \equiv \phi(\zeta = 0, t), \tag{22c}$$

for $\phi > \phi_0$, and $\phi = \phi_0$ otherwise. To calculate $\phi_T(t)$, we consider mass conservation,

$$\frac{\mathrm{d}}{\mathrm{d}t} \int_0^h \phi(z,t)\mathrm{d}z = \frac{\mathrm{d}}{\mathrm{d}t} \int_0^h \phi(\zeta,t)\mathrm{d}\zeta = \int_0^h \frac{\partial \phi}{\partial t}\mathrm{d}\zeta - \phi(h,t) = 0. \tag{23}$$

Consequently, given that ϕ takes a boundary-layer form with $\phi \to \phi_0$ below,

$$\phi_0 \sim \int_0^\infty \frac{\partial \phi}{\partial t}\mathrm{d}\zeta = \frac{D(\phi_T)}{\phi_T} \frac{\partial \phi_T}{\partial t} \int_0^\infty \frac{\phi}{D(\phi)}\mathrm{d}\zeta = \gamma \frac{(\phi_T - \phi_0)}{\phi_T} D(\phi_T) \frac{\partial \phi_T}{\partial t}, \tag{24}$$

by using (21) and the time derivative of (22a). The integral of (24) gives an implicit equation for ϕ_T,

$$\int_{\phi_0}^{\phi_T} (\phi - \phi_0) D(\phi) \frac{\mathrm{d}\phi}{\phi} = \frac{\phi_0}{\gamma} t. \tag{25}$$

Given ϕ_T, the force on the upper boundary is $\Sigma(t) = \Pi_y(\phi_T(t))$, from (16).

Figure 3 shows numerical and asymptotic solutions with $\gamma \ll 1$ for $n = 3$ (Figure 3(a)) and $n = 1.5$ (Figure 3(b)). In both cases, a boundary layer forms at the piston and grows over time as the medium is compressed. For $n = 3$, $D(\phi)$ increases with ϕ at low solidities; the enhancement in diffusivity results in a relatively sharp boundary-layer structure. For $n = 1.5$, $D(\phi)$ decreases with
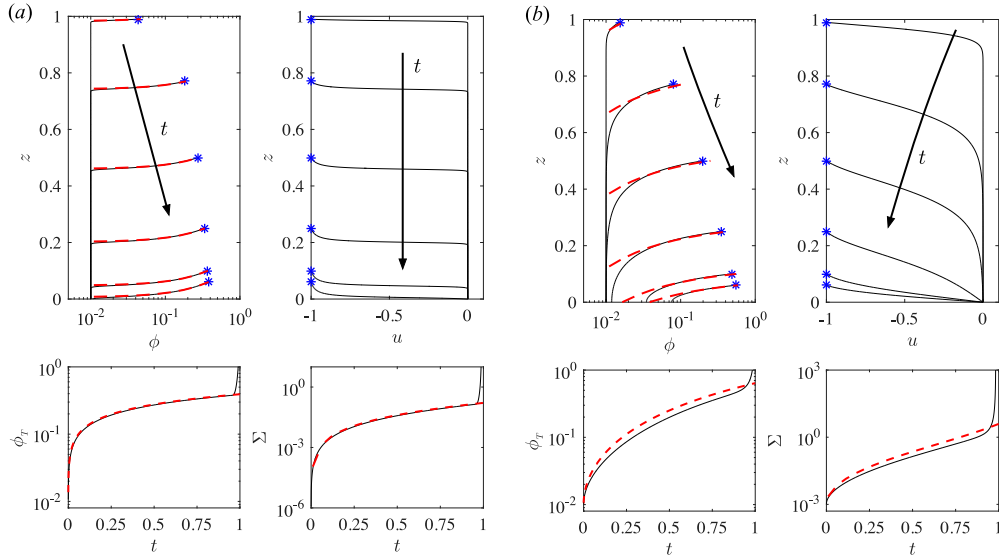
FIG. 3. Results for relatively fast compaction ($\gamma \ll 1$). Numerical solutions (black solid lines) and asymptotic predictions for small γ from (22) and (25) (red dashed lines), for (a) $\gamma = 0.05$ and $n = 3$, and (b) $\gamma = 5 \times 10^{-3}$ and $n = 1.5$. The panels are as in Figure 2, and all results have $\phi_0 = 0.01$. The solid fraction ϕ increases dramatically within the moving boundary layer, below which $\phi(z)$ is almost unchanged from its initial value of ϕ_0 and the suspension remains stationary ($u \approx 0$). Note the rapid increase in ϕ_T and Σ at late times (lower panels), which corresponds to the collision of the boundary layer with the base of the container.

solidity at small ϕ; the local reduction in diffusivity then amplifies the solidity gradient at the piston and the boundary layer is smoother.

As ϕ increases, the boundary-layer solutions become insensitive to the value of n and are instead controlled by whether D remains finite or diverges as $\phi \to 1$. If $D(\phi \to 1)$ remains finite, the solid fraction reaches its maximum value before the piston reaches the bottom boundary, and the force on the piston diverges (Figure 4). Alternatively, if D diverges for $\phi \to 1$, the solid fraction approaches but never reaches its maximum value and the boundary stops compacting. Further depression of the piston then causes the boundary layer to thicken as a growing plug of permeable but essentially incompressible solid. We briefly analyse such "bloated" boundary layer solutions in Appendix A.
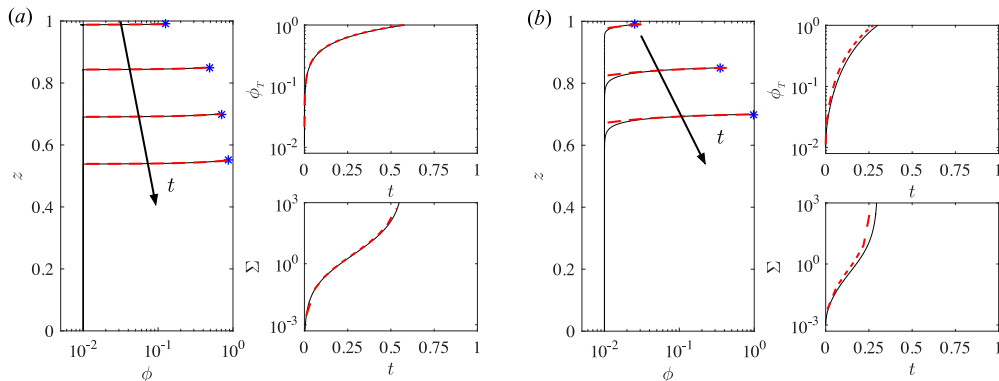

FIG. 4. Solutions of the model (black solid lines) for fast compaction ($\gamma \ll 1$) exhibiting "early time blow up," together with asymptotic predictions for small γ from (22) and (25) (red dashed lines). (a) $\gamma = 5 \times 10^{-3}$ and $n = 3$, and (b) $\gamma = 1 \times 10^{-3}$ and $n = 1.5$. The left-hand panels shows snapshots of $\phi(z)$ at times $t = 0.01$, $t = 0.15$, $t = 0.3$, and $t = 0.45$ ((a) only). The blue star indicates the location of the piston at each time. The right-hand panels show the solid fraction ϕ_T and load Σ at the piston, respectively. In both (a) and (b), the load Σ diverges as $\phi_T \to 1$.

The two possibilities considered in the previous paragraph correspond to different limiting microstructural states of the medium: in the first case, the matrix compresses towards the packing limit whilst leaving voids through which fluid still percolates, i.e., k approaches zero more slowly than p_y diverges, such that $D \to \infty$. For the second situation, the void space becomes disconnected before the matrix is fully compressed, with $k \to 0$ faster than $p_y \to \infty$ so that $D \to 0$. For our fitting functions in (17), which of the two possibilities emerges is dictated by the choices of the exponents a and m.

From a practical perspective, this packing limit lies outside the range of solid fractions for which we are able to measure $k(\phi)$ and $p_y(\phi)$. The values that we will present below for our experiments, for example, are reliable only for smaller values of ϕ. In any event, the choice $\phi = 1$ for the highest attainable solid fraction is presumably unphysical, with maximum packing likely being achieved at a lower solidity. Since our experiments do not stray towards this physical regime, we avoid further theoretical analysis of this limit.

III. EXPERIMENTS

A. Outline of experimental setup

Our main experimental apparatus was a dewatering device that could be programmed to compress a sample of suspension at different speeds whilst measuring the compressive load $\sigma(t)$. We developed a second device to measure the permeability $k(\phi)$ over a comparable range of solid fractions. A brief description of each device is given here; more details can be found in the work of Paterson.[24]

1. Dynamic dewatering device

The dynamic dewatering device, shown schematically in Figure 1(a), was driven using a commercially available material tester (Material Testing Systems 858 Table Top System). A hydraulic actuator with a position sensor was mounted on a frame above a load cell. A permeable piston was attached to the actuator so that it could be pushed down into a cylindrical chamber which contained the suspension and which was set on the load cell. The porosity of the piston was set by a fine-mesh nylon screen, with a hole size of 0.333 mm, and the range of motion of the piston was 100 mm. The load cell had a range of 2.2 MPa of compressive load, when normalized to the piston area. The cylindrical wall of the suspension chamber had an inner diameter of 7.62 cm and depth of 8.5 cm, and was constructed of transparent PVC.

The piston was controlled by a stand-alone motion controller with a LabVIEW interface, capable of actuating speeds from 1 μm/s to 8.33 cm/s. Although this device was programmed to drive a prescribed speed, we observed deviations near the end of the experiment, especially for the faster speeds. To compensate for this in the comparisons between the experiment and theory below, we directly recorded the piston height $\hat{h}(t)$, allowing for any compliance in the apparatus, and input this function directly into the model calculations.

To begin a dewatering experiment, 250 g of a 3–4 wt. % suspension was placed in the dewatering cell. The piston was initially lowered manually to the top of the suspension and this position was recorded (h_0). The piston was then lowered at the set speed; the load was recorded and the experiment halted when a maximum load of 1.3 MPa was exceeded. After each experiment, the compressed suspension was collected and dried to obtain an accurate measurement of the weight of solid, and thus of the original solid fraction of the suspension.

For a given material, we measured the compressive yield stress $p_y(\phi)$ by running experiments at sequentially slower speeds until the measured load as a function of the height of the piston became independent of the speed. In this "quasi-steady" limit, which corresponds to the limit of large γ in our model, the solid fraction is independent of depth (see the analysis of Section II C), and so is given as a function of time from the height of the piston. The raw measurement of the load in this limit corresponds to the compressive stress of the suspension $p_y(\phi)$, plus a contribution from the friction of the piston and the sample on the walls of the chamber and the viscous resistance

of the fluid passing through the piston. Trial experiments with pure fluid in the chamber suggested that the friction force was largely independent of the speed of compression, and thus that the latter contribution was negligible. We therefore estimated the friction for each suspension based on the extrapolated force as $\phi \to 0$. Unless stated otherwise, all the measurements of the load shown in this paper have had the friction force subtracted from them.

Having determined $p_y(\phi)$, we then ran experiments at a range of different compression speeds, which correspond to different values of γ. For each material, at each speed, we performed multiple experiments, to give an average load and variance. We also performed some experiments in which tracer particles with contrasting colour were seeded in the fibre suspension at a concentration of 0.3 wt. %. These experiments were filmed using a high speed camera (Vision Research Phantom V611) with a frame rate fixing apparent speeds to less than 0.01 mm per frame and a field of view set by the initial height of the suspension. A measure of the spatial variation of the solid velocity of the suspension during dewatering was provided by processing the images.

2. Permeability testing apparatus

We developed a separate device to measure the permeability of a suspension over the same range of solid fraction as the dewatering tests. The device, shown schematically in Figure 1(b), consisted of a cylindrical suspension chamber, closed at one end by a permeable cap and at the other end by a permeable piston that could be pushed into the chamber to compress an enclosed sample. The chamber was 10.16 cm in diameter and 16 cm deep, with the piston fully extended, and was connected to a flow loop that circulated fluid through the compressed suspension at a given pressure drop. Both the permeable piston and cap had a fine stainless steel mesh with holes of size 0.28 mm. The piston position was manually controlled by a hydraulic actuator, capable of providing a compressive load of 1 MPa, and located using a linear potentiometer (OMEGA LP801) with a 30 cm range, and with any compliance of the apparatus taken into account. The actual compressive load was measured using a pressure transducer (OMEGA PX309, range 14 MPa) within the actuator, the force of friction on the piston being negligible. The fluid pressure drop across the suspension was measured with a differential pressure transducer (OMEGA PX409, range 1 MPa; no pressure drop was discernible across the permeable piston and cap), and the flow rate determined by disconnecting the loop and using a mass balance and timer. To avoid any effects of air in the fluid on the measurements of the permeability,[28] the flow loop was maintained in a vacuum to reduce dissolved oxygen content to below 5 ppm and was monitored by a dissolved oxygen sensor (Eutech Instruments Alpha DO 500).

Each test was performed by first compressing a sample by a given load. Fluid was then pumped through the sample, and the flow rate and pressure drop measured after the system had equilibrated. The suspension was then compressed by a new (increased) load and the test repeated. After collecting a series of measurements for different loads, we recovered the compressed suspension and again dried the solid mass to obtain its weight.

Flow-induced differential compaction[11] complicates the measurement of permeability in such devices. Here, the spatial variation of ϕ was minimised by ensuring that the compressive load from the permeable piston greatly exceeded the flow-induced compression; see Appendix B. For all our results, we ensured that their ratio lay below 10%.

B. Experimental test materials

We investigated a number of aqueous suspensions of wood pulp, which is composed of cellulose fibres. We present detailed results for a soft wood bleached Kraft pulp (NBSK), diluted to the initial concentration in reverse osmosis water. We also undertook experiments with a hard wood bleach Kraft pulp (HBK) and NBSK pulps that had been treated with commercially available dewatering chemicals to alter the surface charge of the cellulose fibres (see Table I). The dewatering behaviour of the other pulps was similar to the NBSK pulp and we only briefly describe their results below (more detailed results can be found in Paterson[24]).

TABLE I. Physical constants (the average length $\hat{L}$, radius $\hat{r}$ and coarseness $\hat{c}$ (linear density)) and fitting parameters (see (26) and (27)) with their corresponding coefficients of determination (R^2 values) for the various series of experiments conducted. The range of γ over which we ran experiments is also shown. The chemical additive "PL" denotes Eka PL 1510, a linear cationic polyacrylamide, and "PL + NP" denotes an equal combination of Eka PL 1510 and Eka NP 320, which is a colloidal silica solution. For both, the total concentration of chemical added was 0.003% by weight.

Series	Material	Fluid	Additives	Fibre properties			$P_y(\phi)$ fitting					$k(\phi)$ fitting				γ
				$\hat{L}$ (mm)	$\hat{r}(\mu m)$	$\hat{c}$ (mg/m)	m	n	q (MPa)	p_* (kPa)	R^2	a [$(\mu m)^2$]	b	k_* [$(\mu m)^2$]	R^2	
1	Nylon	Glycerine	…	3.05	6.79	1.66	3.73	2.27	2.04	16.2	0.999	6.99	5.40	93.8	0.997	0.010-2.49
2	NBSK	Water	…	2.57	13.34	0.143	2.59	2.13	1.04	10.1	0.999	0.350	18.5	1.27	0.985	0.028-281.46
3	HBK	Water	…	0.79	10.07	0.097	2.19	2.21	1.26	9.79	0.998	0.279	14.06	1.57	0.883	0.030-296.33
4	NBSK	Water	PL	2.57	13.34	0.143	2.55	2.27	1.12	7.87	0.999	0.372	13.7	2.18	0.908	0.032-317.16
5	NBSK	Water	PL + NP	2.57	13.34	0.143	2.56	2.26	1.12	8.06	0.999	0.528	14.3	2.91	0.954	0.043-426.39
6	Polyethylene Foam	Water	…	…	…	…	0.33	2.63	1.05	2.55	0.978	48.8	12.01	338.10	0.987	1.051-4203.23

We also used a suspension of monodisperse nylon fibres in glycerine. Nylon fibres constitute a more idealized fibrous matrix than cellulose, being more uniform in their size distribution and internal structure. Immersing these fibres in glycerine furnished a suspension with dewatering behaviour similar to the cellulose fibre, at least in terms of the magnitude of the compressive load that could be imposed on a sample and the equivalent values of the dimensionless parameter γ. We also investigated a third material, a synthetic polyethylene foam saturated with water, which was less comparable in microstructure with the cellulose pulps; some details and results for this material are given in Appendix C. A summary of physical constants of all the tested suspensions is given in Table I.

C. Constitutive functions

Measurements of the compressive yield stress $p_y(\phi)$ and permeability $k(\phi)$ for the suspensions of NBSK pulp and nylon are shown in Figure 5. The permeability data are replotted in Figure 5(c) after a scaling by the square of the fibre radius $\hat{r}$. Jackson and James[12] have previously found that such scaled permeabilities collapse onto a relatively narrow range for a wide variety of different fibrous materials. Our measurements for nylon fibres lie within their band. However, the permeability of cellulose fibre is significantly lower, and decreases with ϕ rather more steeply. This result is consistent with previous measurements of the permeability of cellulose fibre,[19,25,29] and its physical basis is puzzling, although it is presumably related to the complex structure of cellulose fibres on the micro-scale.

We fit the constitutive functions using the functional forms

$$p_y(\phi) = \frac{q\,\phi^n}{(1-\phi)^m}, \tag{26}$$

$$k(\phi) = \frac{a}{\phi} \log\left(\frac{1}{\phi}\right) \exp(-b\phi), \tag{27}$$

where the parameters p, n, m, a, and b were determined from least-squares fits to the experimental data, and are listed in Table I. Note that we use (27) rather than (17) as the fitting function for the permeability, motivated by the expected limit $k \to \log(1/\phi)/\phi$ for small solid fractions.[12] We further choose to define the dimensional scales k_* and p_* as the values of the permeability and compressive stress at $\phi = 0.1$.
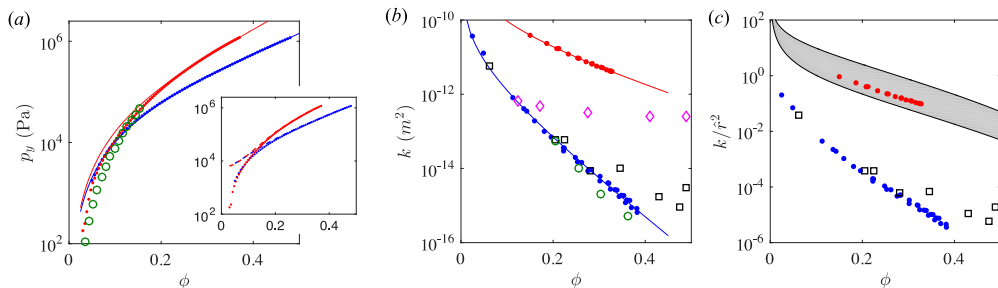

FIG. 5. Experimental measurements of the constitutive functions for nylon fibres in glycerine (red) and NBSK pulp (cellulose fibres) in water (blue), together with some previous measurements of these functions for soft wood pulp suspensions. (a) The compressive yield stress $p_y(\phi)$: the inset shows raw measurements of the load from the slowest dynamic dewatering experiment (dashed lines) and the resulting curve of $p_y(\phi)$ after subtracting the contribution from the friction force (6500 Pa) between the piston and suspension chamber (dots). The main panel shows the same measurements of p_y (dots) together with our fits using (26) (solid lines), and some previous measurements of $p_y(\phi)$ for pulp[30] (green circles). (b) Measurements of $k(\phi)$ from the permeability testing apparatus (dots) and our fits to the data (using (27); solid lines), together with previous measurements of $k(\phi)$ for pulp from the work of Vomhoff[29] (green circles), Pettersson *et al.*[25] (black squares), and Kugge *et al.*[13] (pink diamonds), for comparison. The disagreement of the latter with the other data is discussed in Sec. III C. (c) The same data scaled by the square of the average radius $\hat{r}$ of the fibres (where known). The grey shaded region indicates the range of previous measurements of $k/\hat{r}^2$ for a wide selection of different fibrous materials, as compiled by Jackson and James.[12]
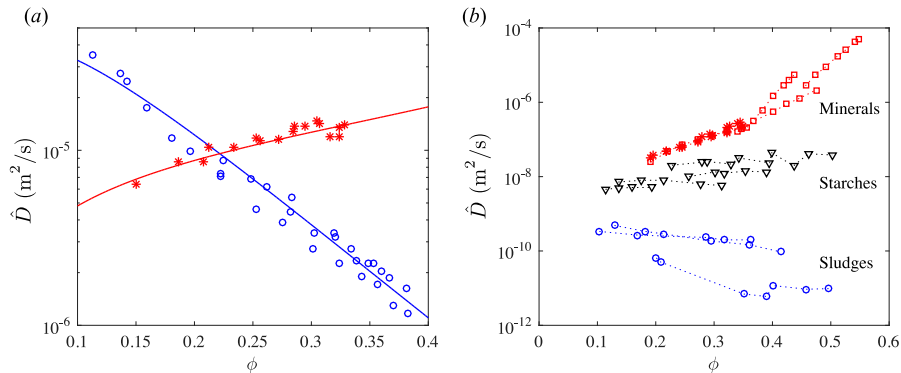
FIG. 6. The dimensional diffusivity function $\hat{D}(\phi) = \phi k(\phi) p'_y(\phi)/\mu$. (a) Our measurements calculated using the data in Figure 5 for nylon fibres in glycerine (red stars) and NBSK cellulose fibres (blue circles), together with the fits calculated using (26) and (27) (solid lines). (b) A compilation of some previous measurements for different materials (mineral suspensions, starches and pulps, and sludges and wastewater, as marked), taken from the work of Stickland and Buscall[27] and de Kretser *et al.*[7]

Given these fits, we calculate the effective diffusivity function of the dewatering model (Sec. II B). Figure 6(a) shows the dimensional form of this function, i.e., $\hat{D}(\phi) = \mu^{-1}\phi k(\phi) p'_y(\phi)$. Interestingly, the diffusivity for cellulose fibre decreases with increasing ϕ while that for nylon increases. The slope of $\hat{D}$ represents a competition between the stiffening of the medium as ϕ is raised and the increased resistance to flow: for nylon, the stiffening of the medium dominates the decrease in permeability; the opposite is true for cellulose fibre. For comparison, Figure 6(b) shows previous measurements of diffusivities for a range of different deformable media, taken from Stickland and Buscall[27] and de Kretser.[7] It is evident that, in general, the diffusivity can both increase or decrease with ϕ.

Note that previous measurements of $k(\phi)$ for cellulose fibres by Kugge *et al.*[13] give a quite different trend with ϕ from our data. These authors extracted their measurements directly from pressure-filtration tests, using a technique that replies on the applicability of a two-phase model like that outlined in Section II. Curiously, the resultant effective diffusivity given by these measurements increases with ϕ, unlike our data for cellulose fibres in Figure 6(a). We will return to this disagreement in Section IV.

D. Experimental results

1. Nylon fibres

Measurements of the load $\sigma(t)$ from experiments with different piston speeds U for the nylon suspension are shown in Figure 7. The results are plotted against both dimensionless time (Figure 7(a)) and the average solid fraction $\overline{\phi}(t) = \phi_0/h(t)$ (Figure 7(b)). As the speed of compression is increased, there is a significant increase in the load for relatively low values of $\overline{\phi}$, while at higher $\overline{\phi}$ the load appears to return towards the quasi-static curve $\sigma = p_y$ (e.g., Figure 7(b), ii-iv). For the fastest speeds, the load becomes so large that it exceeds the experimental threshold before very much dewatering has taken place.

Predictions of the theoretical model, also shown in Figure 7, agree fairly well with the experimental measurements across all the different speeds. The corresponding theoretical profiles of the solid fraction (Figure 8(a)) indicate that the increase in the load for relatively low values of $\overline{\phi}$ corresponds to the formation of a boundary layer below the piston, which is more pronounced at larger speeds. At very late times, the bottom of the boundary layer reaches the base of the container, and the solid fraction of the whole sample increases rapidly, while gradients in ϕ are smoothed out. The corresponding force then increases steeply, while also tending back towards its quasi-static value $p_y(\phi)$, as observed in the measurements of Figure 7. This behaviour results from the fact that the effective diffusivity $D(\phi)$ for nylon increases with ϕ.
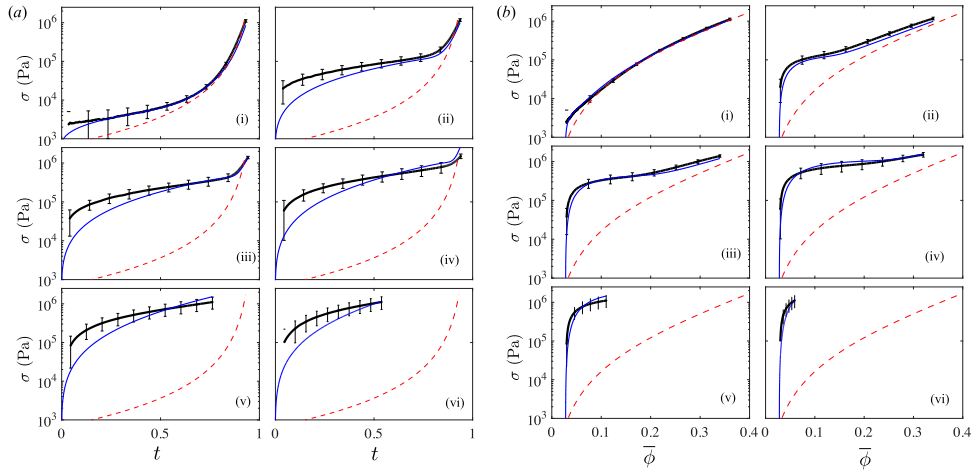
FIG. 7. Average measurements (black solid lines and points) of the load from a suspension of nylon fibres in glycerine, shown (a) as a function of dimensionless time t (related to the dimensional time $\hat{t}$ by $t = h_0 \hat{t}/U$) and (b) as a function of the average solid fraction $\overline{\phi}(t)$ of the suspension, for different speeds U of compression. For each speed, the measurements are averaged over 8 experiments, and the error bars show plus or minus two standard deviations. The different speeds are (i) $U = 0.1$ mm/s, (ii) $U = 1$ mm/s, (iii) $U = 2$ mm/s, (iv) $U = 3$ mm/s, (v) $U = 4$ mm/s, and (vi) $U = 5$ mm/s. Each panel also shows the theoretical prediction (blue solid) and measured compressive yield stress $p_y(\phi)$ (red dashed; in (a) this is plotted as a function of $1 - \phi_0/\overline{\phi}$, which is the dimensionless time for quasi-static compression).

The boundary layer structure of the solid fraction is also reflected in the vertical profile of the solid speed $|u(z,t)|$, which can be compared with data extracted from tracer measurements in the experiments (Figure 8(b)). The tracer measurements for nylon compare satisfyingly with the theoretical predictions. We conclude that the two-phase model appears to provide an adequate description of the dewatering of a nylon suspension, even for relatively fast conditions.
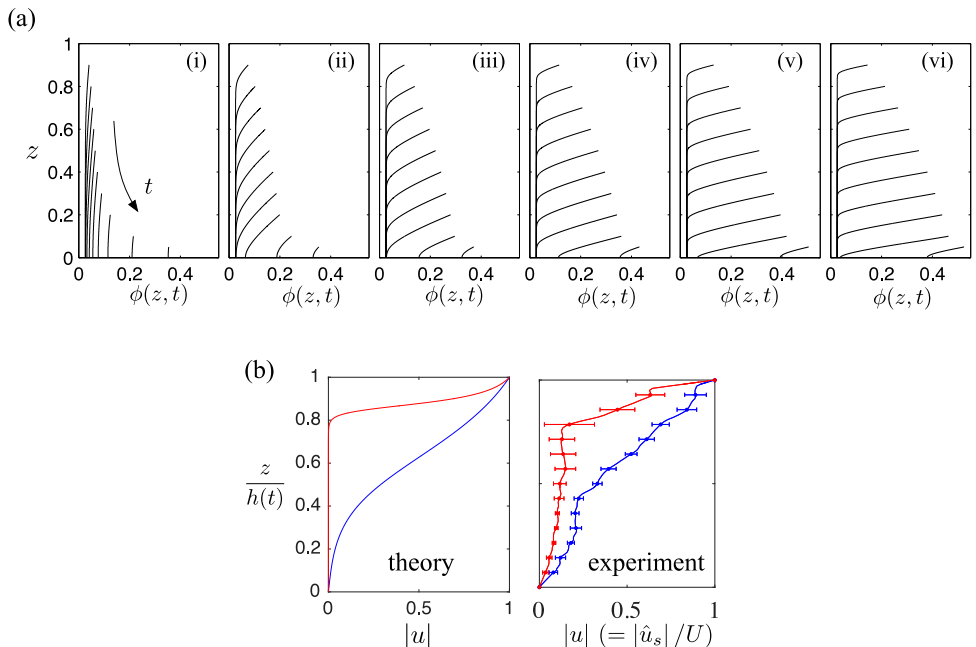

FIG. 8. (a) Model predictions of the solid fraction $\phi(z,t)$ for compression experiments of nylon fibres, at dimensionless times $t = 0.1, 0.2, 0.3, 0.4, 0.5, 0.6, 0.7, 0.8, 0.9$, and 0.95, and for different speeds U. Each panel corresponds to the experiment with the equivalent roman numeral in Figure 7. (b) Snapshots of the predicted dimensionless solid velocity profile and the measured solid velocity profile, as marked, as a function of dimensionless Lagrangian position at time $t = 0.3$ at speed $U = 0.25$ mm/s (blue) and $U = 3$ mm/s (red).
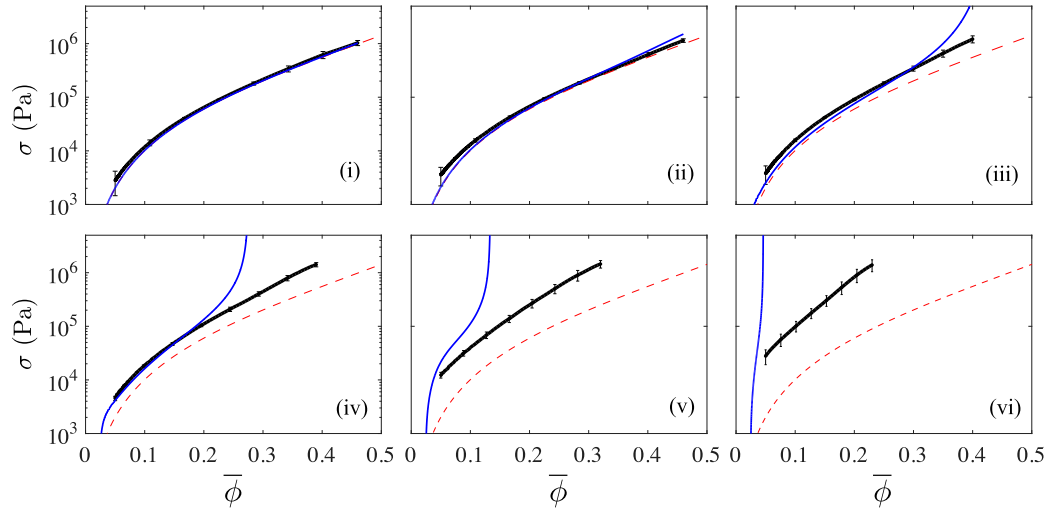
FIG. 9. Average measurements (black solid) of the load from an NBSK pulp suspension in water as a function of the average solid fraction $\overline{\phi}$. For each speed, the measurements are averaged over 4 experiments, and the error bars show plus or minus two standard deviations. The different speeds are: (i) $U = 0.01$ mm/s; (ii) $U = 0.1$ mm/s; (iii) $U = 0.5$ mm/s; (iv) $U = 1.5$ mm/s; (v) $U = 5$ mm/s; and (vi) $U = 10$ mm/s. Each subfigure also shows the measured compressive yield stress $p_y(\phi)$ (red dashed) and the prediction of the theoretical model (blue solid).

2. Cellulose fibres

Measurements from dewatering experiments with the NBSK pulp suspension are shown in Figure 9. Pulp exhibits qualitatively different behaviour from nylon fibres, while the measurements for nylon tended back towards the quasi-static $p_y(\phi)$ curve for large $\overline{\phi}$, for pulp the deviation of the load above p_y increases as $\overline{\phi}$ is increased.

In addition, unlike for nylon, solutions of the model (blue lines in Figure 9) give an increasingly poor agreement with the measurements as the speed is increased. In particular, the model predicts that the load grows much too rapidly with $\overline{\phi}$ at the fastest speeds. Predicted profiles of the solid fraction $\phi(z,t)$ (Figure 10(a)) indicate the root of this diverging load: according to the model, gradients in ϕ that form in the boundary layer below the piston steepen over time, so that, at fast speeds, the solid fraction at the piston rapidly increases and the force diverges. The pronounced build-up of solid into increasingly steep boundary layers below the piston is an inevitable consequence of the fact that the effective diffusivity $D(\phi)$ for pulp decreases as ϕ is increased. However, the measurements of Figure 9 show that this behaviour is not realised in the experiments, with the load remaining much closer to the curve of $p_y(\phi)$ than predicted, and the experiment continuing to compress the suspension long after the model has predicted the divergence of the load.

Further evidence of the difference in model predictions and experimental measurements is provided by a comparison of the solid velocity (Figure 10(b)). For the model at high piston speeds, the solid fraction builds up rapidly into the boundary layer next to the piston while the remainder of the suspension underneath remains stationary (e.g., Figure 10(b): left-hand plots). In contrast, measurements from particle tracking show little discernible difference in structure between fast and slow piston speeds (Figure 10(b): right-hand plots).

We note that the inability of the model to reproduce the dewatering behaviour of cellulose fibres is not simply due to their abnormally low permeability (in relation to other fibres like nylon). A lower permeability would suggest that concentrated boundary layers were more likely to develop below the piston, causing the load to diverge as predicted by the model. Instead, despite the relatively low permeability of the fibres, the solid fraction remains relatively uniform in space. Moreover, the model appears to work quite well for slow dewatering speeds (Figures 9(i) and 9(ii)) and at lower solidities at intermediate speeds (Figures 9(iii) and 9(iv)).
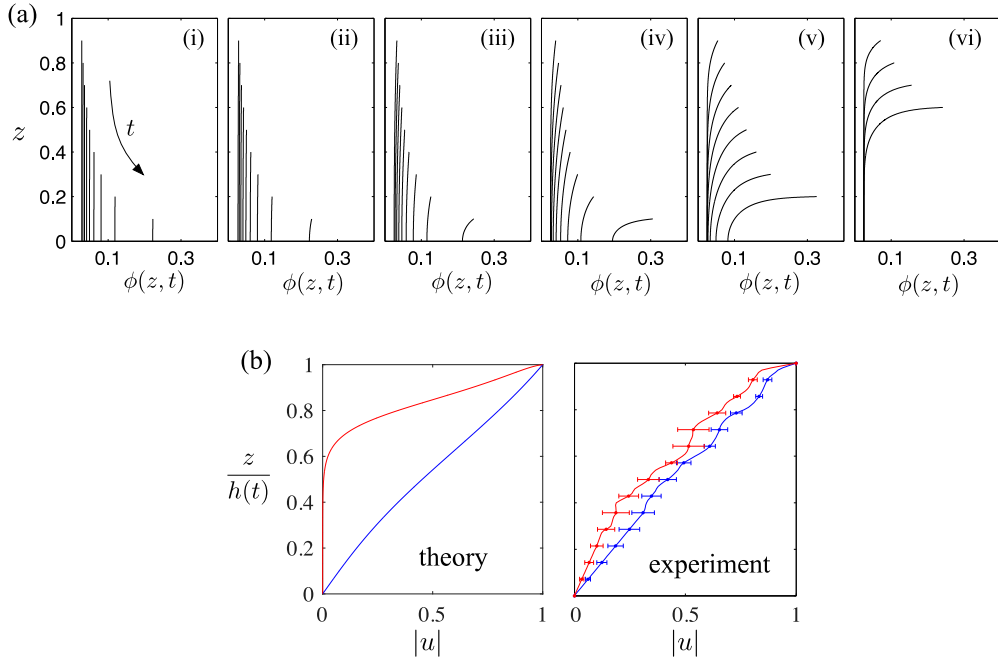
FIG. 10. (a) Predictions of the model of the solid fraction $\phi(z,t)$ for compression experiments of NBSK pulp fibres at dimensionless times $t = 0.1, 0.2, 0.3, 0.4, 0.5, 0.6, 0.7, 0.8,$ and 0.9, and different speeds U. Each panel corresponds to the experiment with the equivalent roman numeral in Figure 9. In panels (v) and (vi), the solid fraction at the piston reaches 1 at dimensionless times $t < 0.9$, at which point the simulation stops. (b) Snapshots of the predicted solid velocity profile and the measured solid velocity profile, as marked, as a function of dimensionless Lagrangian position at time $t = 0.3$ at speed $U = 1.5$ mm/s (blue) and $U = 10$ mm/s (red).

E. Extension to the model

1. The missing ingredient

The failure of the theoretical model to adequately capture the dewatering behaviour of cellulose fibres suggests that some physical ingredient is missing from the model. To identify this omission, we first review some of the basic assumptions.

Our neglect of inertia can be validated by estimating the pore-scale Reynolds number, $U\sqrt{k_*}/\mu$, which is always less than 0.01 for the pulp suspensions (and much less for nylon suspensions). The importance of gravity can be estimated from $\Delta\rho g\hat{h}/p_* \approx 0.1$, where $\Delta\rho$ is the fluid-solid density difference, which is again small. The importance of viscous stresses in the fluid phase is gauged by the Darcy number $Da = k/\hat{r}^2$, which is order one for the nylon suspension but definitely small for the cellulose fibres (see Figure 5(c)). Thus, none of these effects is likely to be responsible for the discrepancy between the model and experiments.

However, the assumption that the rheology of the suspension is determined purely by the local solid fraction - as in (8) - may be more suspect, owing to the microstructure of cellulose fibres. In particular, these fibres are long, thin, hollow tubes filled with water, with weakly permeable walls.[23] As the suspension is compressed, two main process take place, both of which result in an increase in the solidity and strength of the solid matrix: the fibres rearrange and deform to form a closer packing, and some of the liquid contained within the fibres is squeezed out. The former process might plausibly be strain dependent (and thus solidity dependent). The latter, however, is rate dependent because of the viscous resistance generated when the excess applied compressive stress forces fluid trapped inside the fibres to flow through the permeable walls, reducing the size of the fibre and increasing the solid fraction. The relation between the excess applied pressure and the transient increase in ϕ suggests a dimensional rheology of the form

$$\frac{D\phi}{D\hat{t}} \equiv \frac{\partial\phi}{\partial\hat{t}} + \hat{u}_s\frac{\partial\phi}{\partial\hat{z}} = \lambda(\phi)\left[\mathcal{P} - p_y(\phi)\right], \tag{28}$$

for some bulk compressibility function $\lambda(\phi)$ that depends on the permeability of the fibre wall and the fluid viscosity. Unlike cellulose, nylon fibres are relatively rigid and not hollow, and it seems reasonable to neglect this rate-dependent process, so that $\mathcal{P} = p_y(\phi)$ for the nylon suspension.

An equation of the form (28) was proposed by Buscall and White[4] and has been cited by various authors since[5,14,15] as a phenomenological constitutive law to describe plasticity of the solid phase when the compressive stress exceeds the yield stress. However, these authors typically argue that λ is large, and so recover $\mathcal{P} = p_y$. An alternative expression of (28), using (1), is

$$\mathcal{P} = p_y(\phi) - \frac{\phi}{\lambda(\phi)}\frac{\partial \hat{u}_s}{\partial \hat{z}}, \tag{29}$$

which can be interpreted as a generalised visco-plastic constitutive equation with bulk solid viscosity ϕ/λ, and is similar in form to rheological expressions used in geophysics to describe viscous compaction.[10,20,26] More generally, expressions of a similar form to (29) have been recovered from measurements of the bulk rheology of suspensions of rigid particles.[2]

2. The improved model

Introducing (29) into (6) and (7) leads to a differential equation for the solid velocity,

$$\hat{u}_s = -\frac{k(\phi)}{\mu}\left[p'_y(\phi)\frac{\partial \phi}{\partial \hat{z}} - \frac{\partial}{\partial \hat{z}}\left(\frac{\phi}{\lambda(\phi)}\frac{\partial \hat{u}_s}{\partial \hat{z}}\right)\right], \tag{30}$$

in place of the explicit expression in (9). In dimensionless form, the model equations are then revised to

$$\frac{\partial \phi}{\partial t} = -\frac{\partial}{\partial z}(\phi u) \qquad \text{and} \tag{31a}$$

$$u + \gamma\frac{D(\phi)}{\phi}\frac{\partial \phi}{\partial z} = \varepsilon K(\phi)\frac{\partial}{\partial z}\left[\Lambda(\phi)\frac{\partial u}{\partial z}\right], \tag{31b}$$

where $\Lambda(\phi) = \phi\lambda_*/\lambda(\phi)$ with λ_* being a dimensional compressibility scale, and the dimensionless parameter $\varepsilon = k_*/(\mu h_0^2\lambda_*)$ is a ratio of the timescale for relaxation of the network to that for pore pressure diffusion. The effective bulk viscosity of the network also contributes to the load on the piston,

$$\Sigma(t) = \Pi_y(\phi(h,t)) - \varepsilon\frac{\Lambda(\phi(h,t))}{\gamma}\left.\frac{\partial u}{\partial z}\right|_{z=h}, \tag{32}$$

(recall that $\partial u/\partial z \leqslant 0$). Our original model is recovered in the limit $\varepsilon = 0$.

In general, irrespective of the form of $\Lambda(\phi)$, the net effect of the new term on the right-hand side of (31b) is to reduce spatial gradients in solid velocity, and therefore solid fraction. Numerical solutions of the revised model shown in Figure 11 illustrate this behaviour: Figure 11(a) shows how the solid fraction becomes increasingly smoothed as ε is increased. Simultaneously, the load on the piston is reduced (Figure 11(c)) because of the decrease in the compressive stress $\Pi_y(\phi)$ at the surface. However, for larger values of ε, the load becomes larger because the bulk viscous stress of the network eventually dominates the resistance to compression (dashed lines in Figure 11(c)).

A quantitative comparison of the revised model with the experimental results for pulp requires a choice for the bulk compressibility function $\lambda(\phi)$, which we have not attempted to measure. Instead, we use a crude model for the flow out of an individual cylindrical fibre. Given a hollow fibre with wall permeability k_f and radius $\hat{r}$, we estimate a Darcy flux across the fibre wall per unit length of $\hat{v} \sim k_f\Delta\hat{p}/(\hat{r}\mu)$. The relevant pressure difference here, $\Delta\hat{p}$, is the excess network pressure above the compressive strength of the medium, averaged over the scale of the fibres, such that $\phi\Delta\hat{p} = (\mathcal{P} - p_y)$. If the change in fibre radius due to the Darcy flux is linearly related to a change in strain, and thus in solid fraction, then $\Delta\hat{p} \sim (\hat{L}\hat{r}\mu/k_f)D\phi/D\hat{t}$, where $\hat{L}$ is the characteristic length of the fibre. Thus $\lambda \propto \phi^{-1}$, or equivalently $\Lambda = \phi^2$.

Comparison of the predictions of the extended model with the experimental results for pulp (Figure 12(a)) shows that the model now predicts the same qualitative behaviour as the experiments,
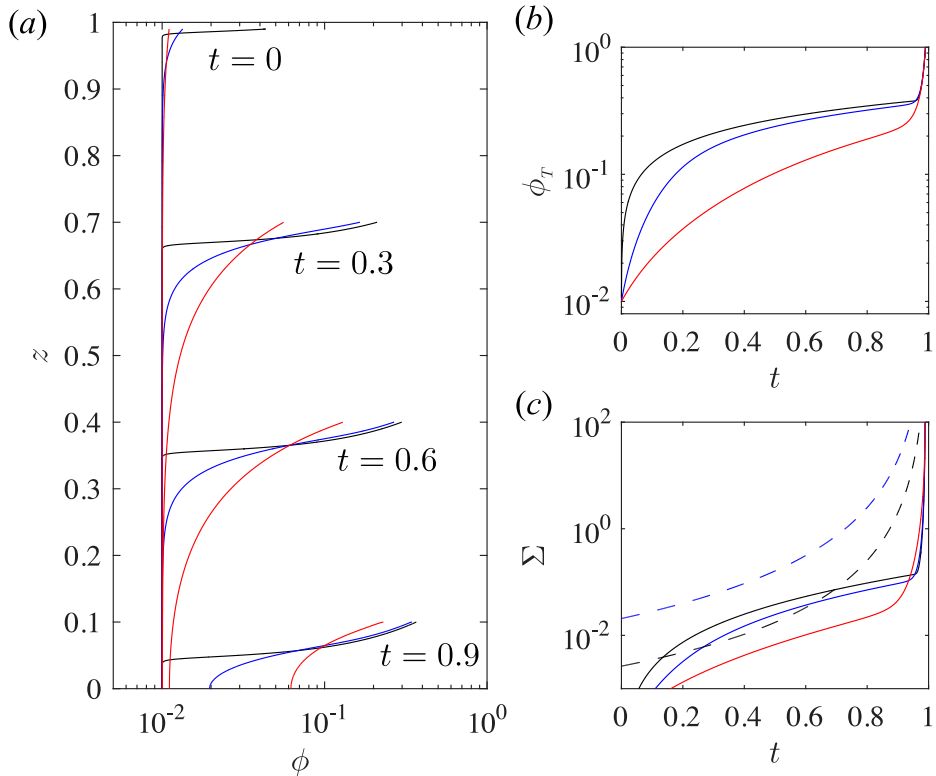
FIG. 11. Example solutions of the model with $\gamma = 0.05$, $n = 3$, and $\phi_0 = 0.01$, as in Figure 3(a), for $\Lambda = \phi^2$ (i.e., $\lambda = \lambda_*/\phi$) and $\varepsilon = 0$ (black), $\varepsilon = 1 \times 10^{-3}$ (blue), and $\varepsilon = 1 \times 10^{-2}$ (red). (a) Snapshots of the solid fraction at different times as marked. (b) The solid fraction at the piston. (c) The load on the piston, together with additional solutions for $\varepsilon = 1$ (black dashed) and $\varepsilon = 10$ (blue dashed).
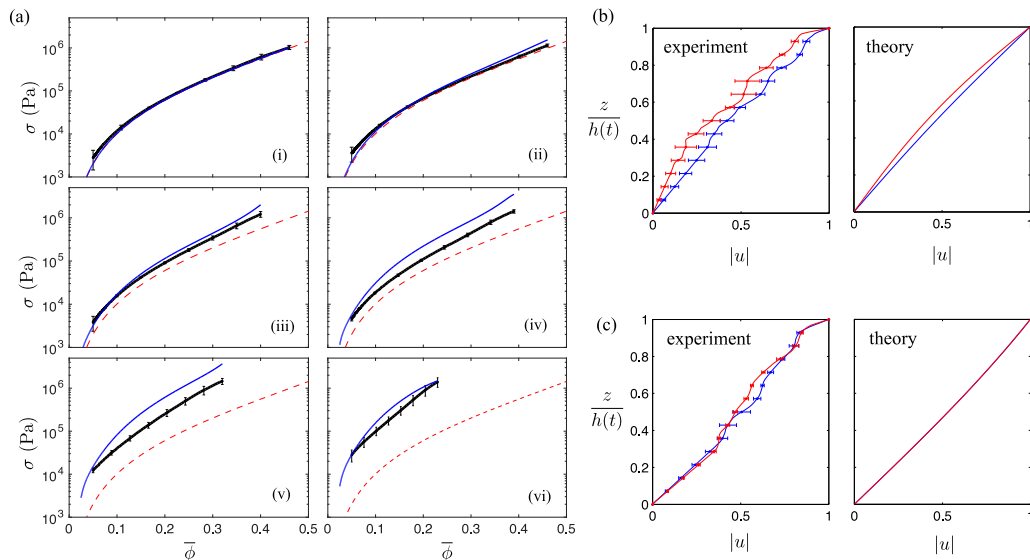

FIG. 12. Measurements of the load for softwood (NBSK) pulp suspensions at different compression speeds as in Figure 9, together with the predictions of the revised model (blue) with $\Lambda = \phi^2$ (i.e., $\lambda = \lambda_*/\phi$) and $\varepsilon = 7$. ((b) and (c)) Measurements of the solid velocity from particle tracking at dimensionless times (b) $t = 0.3$ and (c) $t = 0.6$, together with predictions of the revised model as marked, at speeds $U = 1.5$ mm/s (blue; corresponding to panel iv) and $U = 10$ mm/s (red; corresponding to panel vi).

provided the free parameter ε is suitably chosen. In particular, the rapid divergence of the load at faster speeds (observed in the predictions of Figure 9) is suppressed by the inclusion of the viscous compaction term, given a suitable choice of ε. The revised model also gives a much improved prediction of the solid velocity profiles for different piston speeds (Figures 12(b) and 12(c)) (cf. the previously poor agreement in Figure 10(b)). We note that other forms of $\Lambda(\phi)$ give similar qualitative improvement to the agreement between model and experiment (given a suitable choice of ϵ), which supports the inclusion of the rate-dependent term if not necessarily the chosen form.

The inclusion of the new term in the model does not just influence the resulting load at large piston speeds and higher solidities. The new term also effects a fundamental change to the early time solution of the model, owing to the elliptic character of the equation for the solid velocity (31b). In particular, for experiments with a fixed rate of compression, this will result in a reduction in the rate at which the solidity increases from the scaling of $t^{1/2}$ in the original model (e.g., Ref. 15). A similar change is rendered in the case of experiments with a fixed load, which will almost certainly impact the inference of permeability using established techniques that exploit the time-dependence of the model (e.g., Ref. 16).

3. Goodness of fit

A more systematic measure of the agreement between model and experiment is provided by a dimensionless "goodness of fit parameter" θ, which quantifies the discrepancy between model predictions and experimental measurements of the load as a function of the solidity. For a given piston speed U, we define θ by the integral of the squared difference between the measured load curve $\sigma_{exp}(\overline{\phi})$ and prediction $\sigma_{theory}(\overline{\phi})$,

$$\theta^2(U) = \frac{1}{\phi_b - \phi_a} \int_{\phi_a}^{\phi_b} \left(\log\left[\sigma_{exp}(\overline{\phi})\right] - \log\left[\sigma_{theory}(\overline{\phi})\right] \right)^2 d\overline{\phi}, \tag{33}$$

where ϕ_a and ϕ_b denote the minimum and maximum value of $\overline{\phi}$ in the experiment. Smaller values of θ correspond to a better agreement between theory and experiment, whereas θ diverges if the theoretical load diverges before the experimental load reaches its maximum allowed value.

Figures 13(a) and 13(b) show θ for the nylon fibres and NBSK pulp suspensions. For nylon, the agreement between experiment and theory with $\varepsilon = 0$ was very good: $\theta < 0.15$ for all speeds (Figure 13(a)). For pulp, on the other hand, the agreement was very poor at the fastest speeds, as reflected by the divergence of θ there (Figure 13(b)). The introduction of the viscous compaction term gives a clear improvement at the fastest speeds (Figure 13(b), blue circles).

Similar results were obtained for the other cellulose samples that we tested (see Sec. III B). In all cases, the original model was qualitatively wrong at the fastest speeds, whereas the inclusion of the viscous compaction term significantly improved the comparison of model and experiment; see Figures 13(c) and 13(d). Indeed, we were able to bound the goodness-of-fit parameter by $\theta < 1$
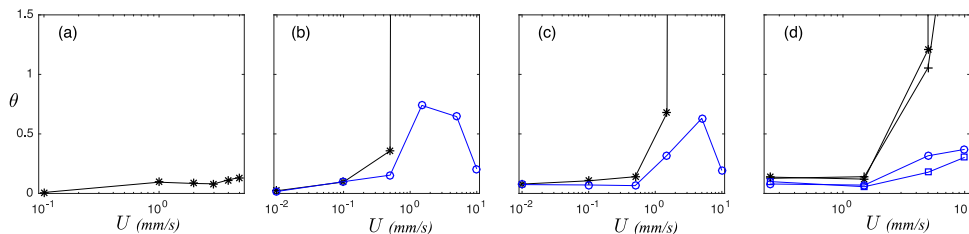

FIG. 13. The goodness-of-fit parameter θ defined in (33), which measures the agreement between the theory and experiments, for different materials. Solid black symbols indicate that $\varepsilon = 0$ in the model; open blue symbols indicate that $\varepsilon > 0$, roughly chosen by eye to minimise θ in each case. In all calculations with $\varepsilon > 0$, we use $\Lambda = \phi^2$. (a) Nylon fibres in glycerine. (b) NBSK cellulose fibres in water (blue circles: $\varepsilon = 7$). (c) HBK cellulose fibres in water (blue circles: $\varepsilon = 5.6$). (d) Two different chemically treated NBSK pulps in water: the main qualitative effect of the chemicals in either case was to increase the permeability of the suspension. The chemicals were PL (stars and circles: $\varepsilon = 2.9$) and PL + NP (crosses and squares: $\varepsilon = 1.9$).

across all speeds of compression by the inclusion of a viscous compaction term with the values of ε given in the caption.

Finally, we note that the results of experiments that we conducted with synthetic foam (see Appendix C) were more like those for pulp than for nylon: again we found that the model with $\varepsilon = 0$ predicted the wrong qualitative behaviour for the fastest speeds of compression and that the revised model significantly improved the predictions. This is especially curious given the evident microstructural differences between the two materials, which one might have expected to rule out our parameterization of the viscous compaction term. Perhaps the form of this addition to the theoretical model belies a more general and widely applicable nature.

IV. CONCLUDING REMARKS

In this paper, we have provided a combined theoretical and experimental study of the relatively rapid dewatering of fibrous suspensions. Our theoretical model is similar to existing models, although we have focussed on dewatering with a fixed rate of compression, rather than the more commonly studied case of fixed load, and provided a selection of numerical and asymptotic solutions. The model requires two constitutive functions to describe the compressive yield stress and permeability of the suspension. Our experiments were designed to calibrate these functions and then perform rapid dewatering tests to compare with the theoretical model. Having measured the constitutive functions, the theory contains no adjustable parameters, which enables us to test unambiguously the model against the experiments.

We found that the predictions of the model provide a reasonable agreement with experiments for a suspension of nylon fibres in glycerine. By contrast, the model performs poorly for aqueous suspensions of wood pulp, particularly under conditions of rapid compression. We have attributed this poor agreement to the microstructure of saturated pulp fibres, which are hollow, fractured, elongated capsules that are filled with liquid. As for the suspension of solid, relatively rigid nylon, slow compression of the pulp suspension forces rearrangement and deformation of the fibres in a rate-independent fashion. However, for faster compression the fluid contained within the pulp fibres begins to leak out, leading to a rate-dependent stress that we have suggested has analogy with plastic deformation or viscous compaction of the solid matrix. This led us to modify the model, which resulted in a significant improvement in comparison with the pulp experiments.

Our conclusion that one needs to include a rate-dependent stress in the dewatering theory for certain materials has consequences for the techniques that have been developed to measure permeability using pressure filtration,[5,14,16] which exploit a short-time solution of the two-phase model. That solution must be revised to incorporate the new stress in order to properly extract the permeability (or hindered-settling function) from a fixed-load experiment. Indeed, the new term changes the nature of the early time solution of the model and will break the scaling with $t^{1/2}$ on which these techniques rely. We suspect that this issue lies at the heart of the significant discrepancy between both our and previous measurements of the permeability of cellulose fibres[25,29] and measurements by Kugge *et al.*,[13] which decrease far less dramatically with solidity (see Figure 5(b)). Indeed, Kugge's data leads to an effective diffusivity for cellulose that increases with ϕ, rather than decreases as we report here, which would result in qualitatively different model predictions.

APPENDIX A: "BLOATED BOUNDARY LAYER" SOLUTIONS OF THE MODEL FOR $\gamma \ll 1$

When the solid fraction near to the piston approaches a hypothetical limiting value ϕ_{max} in the limit $\gamma \ll 1$, further compaction either forces ϕ to attain its limit, such that the force diverges and the

model breaks, or else the solid fraction saturates and the boundary layer migrates ahead of the piston. These two limits correspond, respectively, to a finite limiting diffusivity $D(\phi_{max})$, as considered in Figure 4, or a diverging diffusivity $D \to \infty$ as $\phi \to \phi_{max}$. We consider the latter situation here, by introducing a slightly modified constitutive law for the dimensionless network pressure,

$$\Pi_y = \frac{\phi^n}{(1 - \phi/\phi_{max})^m}, \tag{A1}$$

such that force required to compress the medium diverges at some $\phi_{max} < 1$, while the permeability remains non-zero. The effective diffusivity is again $D(\phi) = \phi \Pi_y'(\phi) K(\phi)$.

We proceed in an analogous fashion to the analysis of Sec. II C 2 in the main text, by neglecting $\partial \phi / \partial t$ and transforming into a frame moving with the edge of the boundary layer, which is assumed to propagate ahead of the piston. If the edge of the boundary layer is located a distance $b(t)$ ahead of the piston, which is itself at $z = h(t) = 1 - t$, we set $z = h - b - \zeta$, and (13) reduces to

$$\left(1 + \frac{\partial b}{\partial t}\right) \frac{\partial \phi}{\partial \zeta} \sim -\gamma \frac{\partial}{\partial \zeta} \left[D(\phi) \frac{\partial \phi}{\partial \zeta}\right]. \tag{A2}$$

We integrate (A2) and impose both $\phi = \phi_T$ and $u = -1$ (or $\gamma D(\phi) \partial \phi / \partial \zeta = -\phi$) at the piston, and $\phi \to \phi_0$ and $u \to 0$ (or $D(\phi) \partial \phi / \partial \zeta = 0$) outside the moving boundary layer, to give

$$\frac{\phi_T (\phi - \phi_0)}{\phi_T - \phi_0} \sim -\gamma D(\phi) \frac{\partial \phi}{\partial \zeta}, \tag{A3}$$

which can be integrated again to give $\phi(z,t)$. The unknown $\phi_T(t)$ is determined from mass conservation by

$$\phi_0 (1 - h) = \int_0^h (\phi - \phi_0) \, dz \sim \gamma \frac{(\phi_T - \phi_0)}{\phi_T} \int_{\phi_0}^{\phi_T} D(\phi) d\phi, \tag{A4}$$

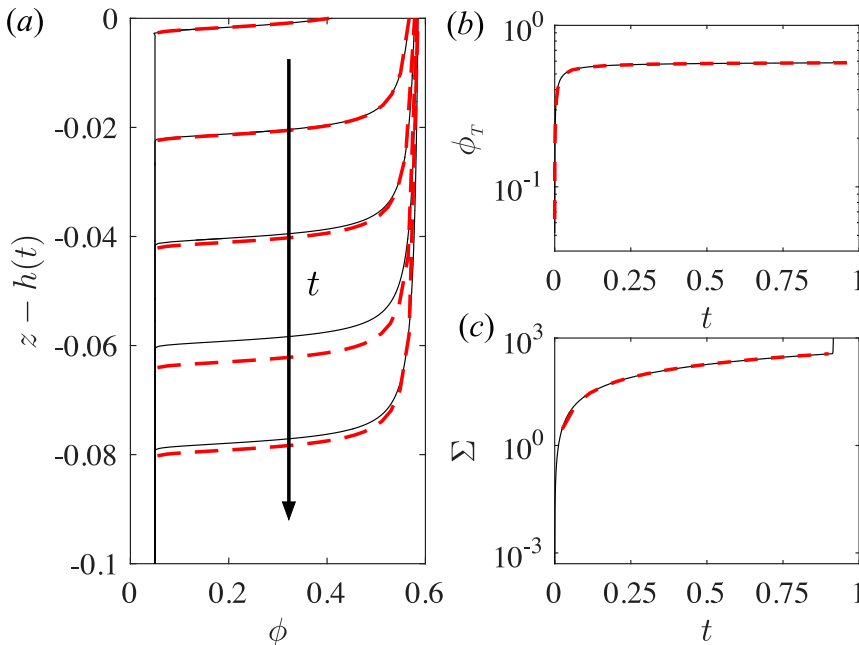using (A3). Example solutions with a bloated boundary layer are shown in Figure 14.

FIG. 14. Numerical solutions (black lines) for $\gamma = 1 \times 10^{-3}$, $\phi_0 = 0.05$, $n = 3$, and $\phi_{max} = 0.6$ showing the build-up of a "bloated boundary layer" below the piston, together with the asymptotic theory (red dashed lines). (a) The solid fraction ϕ in co-ordinates moving with the piston, at times $t = 0.01, 0.2, 0.4, 0.6,$ and 0.8; (b) the solid fraction ϕ_T at the piston, which rapidly approaches ϕ_{max}; and (c) the load Σ on the piston. The sudden increase in Σ corresponds with the arrival of the bloated boundary layer at the bottom boundary.

APPENDIX B: CALCULATION OF THE PERMEABILITY $k(\phi)$

Both our current results and existing results in the literature[25,29] indicate that the permeability of cellulose fibres is substantially lower than that of other fibrous, porous media as given by Jackson and James[12] (see Figure 5). This being the case, we have developed an independent methodology to determine the permeability of a deformable suspension without *a priori* knowledge of the rheology of the suspension or of its dependence on the solid volume fraction or strain rate. The methodology proposed below defines simple experimental criteria for which the effects of differential compaction are avoided, thus allowing k to be determined using a simple Darcy experiment of permeating flow through a compressed suspension.

We consider steady flow with a flux per unit area of Q, driven by a hydraulic pressure difference $\Delta\hat{p}$, across a two-phase deformable suspension of depth H and average solid fraction $\overline{\phi} = \int_0^H \phi \, d\hat{z}$ that is under an external mechanical load σ. From (3),

$$k\frac{\partial p_y}{\partial \hat{z}} = -Q\mu, \qquad p_y\big|_{\hat{z}=0} = \sigma + \Delta\hat{p}, \quad p_y\big|_{\hat{z}=H} = \sigma. \tag{B1}$$

Note that, since the flow is steady, additional strain-rate dependent contributions to the rheology of the suspension, as discussed in Sec. III E, do not play a role here. Since $\partial p_y/\partial\hat{z} = p_y'(\phi)\partial\phi/\partial\hat{z}$, we introduce a pressure scaling of $p_y'(\overline{\phi})$ and set,

$$z = \frac{\hat{z}}{H}, \qquad K = k\frac{\Delta\hat{p}}{Q\mu H}, \qquad P = \frac{p_y - \sigma}{p_y'(\overline{\phi})}, \quad \text{and} \quad \delta = \frac{\Delta p}{p_y'(\overline{\phi})}. \tag{B2}$$

Equation (B1) becomes

$$K\frac{\partial P}{\partial z} = -\delta, \qquad P = \delta \text{ at } z = 0; \qquad P = 0 \text{ at } z = 1. \tag{B3}$$

If $\delta \ll 1$, then $\partial\phi/\partial z \ll 1$, which is the desired limit. We then expand as

$$\phi(z) = \overline{\phi} + \delta\phi_1(z) + O(\delta^2), \qquad K = K_0(\phi) + \delta K_1(\phi) + O(\delta^2), \qquad P = P_0(\phi) + \delta P_1(\phi) + O(\delta^2), \tag{B4}$$

so that $\int_0^H \phi_i \, dz = 0$ for all $i \geqslant 1$.

The leading-order balance in (B3) gives

$$K_0(\overline{\phi})\frac{\partial P_0(\overline{\phi})}{\partial z} = 0; \quad P_0 = 0 \quad \text{at} \quad z = 0, 1 : \quad \implies \quad P_0(\overline{\phi}) = 0, \tag{B5}$$

while at $O(\delta)$,

$$K_0(\overline{\phi})\frac{\partial}{\partial z}\left[P_1(\overline{\phi}) + \phi_1 P_0'(\overline{\phi})\right] = -1, \tag{B6}$$

which can be integrated using the boundary conditions to give

$$K_0(\overline{\phi}) = 1, \quad P_1(\overline{\phi}) = \frac{1}{2} \qquad \text{and} \qquad \phi_1(z) = \frac{1}{P_0'(\overline{\phi})}\left(\frac{1}{2} - z\right). \tag{B7}$$

At $O(\delta^2)$,

$$K_1 + \phi_1 K_0' = \frac{\partial}{\partial z}\left[P_2 + \phi_1 P_1' + \phi_2 P_0' + \frac{\phi_1^2}{2}P_0''\right], \tag{B8}$$

where all the terms are evaluated at $\phi = \overline{\phi}$. The quantity inside the brackets on the right-hand side of (B8) must vanish at $z = 0$ and $z = 1$, as must the integral of ϕ_1, which implies that $K_1(\overline{\phi}) = 0$.

Noting that $P'_0(\overline{\phi}) = P'(\overline{\phi}) + O(\delta) = 1 + O(\delta)$ from the definition of P, and converting back into dimensional variables, the expansions are

$$\phi = \overline{\phi} + \frac{\Delta\hat{p}}{p'_y(\overline{\phi})}\left(\frac{1}{2} - \frac{\hat{z}}{H}\right) + O(\delta^2), \tag{B9a}$$

$$k(\phi) = \frac{Q\mu H}{\Delta\hat{p}}\left[1 + \left(\phi - \overline{\phi}\right)k'_0(\overline{\phi}) + O(\delta^2)\right], \tag{B9b}$$

$$p_y(\phi) = \sigma + \frac{\Delta\hat{p}}{2} + p'_y(\overline{\phi})\left[\phi - \overline{\phi} + O(\delta^2)\right], \tag{B9c}$$

where k'_0 is undetermined. Thus, by evaluating solutions at $\hat{z} = H/2$, we have $\phi = \overline{\phi}$ and $k = Q\mu H/\Delta\hat{p}$, accurate to $O(\delta^2) = O([\Delta\hat{p}/p'_y(\overline{\phi})]^2)$ rather than to $O(\delta)$ as might first be expected.

This analysis indicates how to generate accurate measurements of the permeability. For a given sample, measurements can be taken by first setting the external load σ, which determines H and thus $\overline{\phi}$ from mass conservation. Then, for different fluid pressure differences $\Delta\hat{p}$, one can directly measure the flow rate per unit area Q, and thus the leading-order permeability $k = Q\mu H/\Delta\hat{p}$. The error in this measurement of $k(\overline{\phi})$ is of order $(\Delta\hat{p}/p'_y(\overline{\phi}))^2$, where $p_y(\phi)$ is assumed to be a known function (e.g., previously measured using a different machine). In fact, even if p_y is not already known, it could in principle be measured directly using (B9c), by $p_y(\overline{\phi}) = \sigma + \Delta\hat{p}/2 + O\left([\Delta\hat{p}/p'_y(\overline{\phi})]^2\right)$, and then the magnitude of $\delta = \Delta\hat{p}/p'_y(\overline{\phi})$ could be checked *post hoc*. For all our test materials, measurements of $p_y(\phi)$ using this approach were in rough agreement with direct measurements from the dynamic dewatering device.

APPENDIX C: FOAM EXPERIMENTS

We also carried out a series of experiments using a commercially available, relatively stiff, polyethylene foam saturated in water, and we briefly present the results here for comparison. Figures 15(a) and 15(b) show the measured permeability and effective diffusivity for foam; like
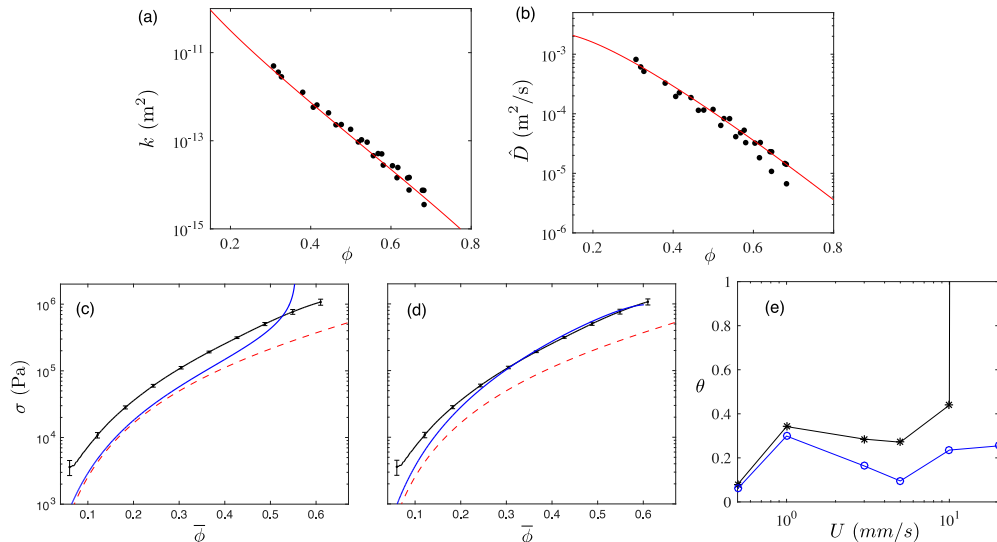

FIG. 15. Results for polyethylene foam in water. (a) The measured permeability $k(\phi)$ and (b) the calculated dimensional diffusivity $\hat{D}(\phi)$, together with fits to the data of the form (26) and (27) with parameters quoted in Table I. ((c) and (d)) Measurements of the load at speed $U = 20$ mm/s (black solid), averaged over four experiments, together with the measured compressive yield stress $p_y(\phi)$ (red dashed) and the prediction of the model (blue solid) with: (c) $\varepsilon = 0$ and (d) $\varepsilon = 20$. This speed corresponds to a value of $\gamma = 1.1$. (e) The goodness-of-fit parameter $\theta(U)$ defined in (33) for the model with $\varepsilon = 0$ (black stars) and $\varepsilon = 20$ (blue circles). All simulations with $\varepsilon > 0$ have $\Lambda = \phi^2$.

pulp, the diffusivity decreases with ϕ. Measurements of the load $\sigma(\overline{\phi})$ under fairly rapid compression are shown in Figure 15(c), together with predictions of the model. Even though the parameter γ is not particularly small at this speed ($\gamma = 1.1$), there is an evident difference between the experimental measurements and the model predictions. Interestingly, as with pulp, the inclusion of a viscous compaction term in the model ($\varepsilon > 0$) leads to a clear improvement (Figure 15(d)), and this result applies across a range of compression speeds, as illustrated by the goodness-of-fit parameters in Figure 15(e). This observation suggests that the inclusion of a rate-dependent term in the model may be appropriate even in situations where there is no clear micro-structural basis for it, and highlights the importance of further study into the role of rate-dependence in the dynamics of dense suspensions.

[1] Audet, D. M. and Fowler, A. C., "A mathematical model for compaction in sedimentary basins," Geophys. J. Int. **110**(3), 577–590 (1992).

[2] Boyer, F., Guazzelli, E., and Pouliquen, O., "Unifying suspension and granular rheology," Phys. Rev. Lett. **107**, 188301 (2011).

[3] Bürger, R., Concha, F., and Karlsen, K., "Phenomenological model of filtration processes. I. Cake formation and expression," Chem. Eng. Sci. **56**(15), 4537–4553 (2001).

[4] Buscall, R. and White, L. R., "The consolidation of concentrated suspensions. I. The theory of sedimentation," J. Chem. Soc., Faraday Trans. 1 **83**, 873–891 (1987).

[5] De Kretser, R. G., Boger, D. V., and Scales, P. J., "Compressive rheology: An overview," Rheol. Rev. **1**, 125–166 (2003).

[6] De Kretser, R. G., Scales, P. J., and Boger, D. V., "Improving clay-based tailings disposal: Case study on coal tailings," AIChE J. **43**, 1894–1903 (1997).

[7] de Kretser, R. G., Usher, S. P., Scales, P. J., Boger, D. V., and Landman, K. A., "Rapid filtration measurement of dewatering design and optimization parameters," AIChE J. **47**(8), 1758–1769 (2001).

[8] Fitt, A. D., Howell, P. D., King, J. R., Please, C. P., and Schwendeman, D. W., "Multiphase flow in a roll press nip," Eur. J. Appl. Math. **13**(03), 225–259 (2002).

[9] Fowler, A., *Mathematical Geoscience* (Springer, 2011), Vol. 36.

[10] Fowler, A. C. and Yang, X., "Pressure solution and viscous compaction in sedimentary basins," J. Geophys. Res.: Solid Earth **104**(B6), 12989–12997, doi:10.1029/1998JB900029 (1999).

[11] Hewitt, D. R., Nijjer, J. S., Neufeld, J. A., and Worster, M. G., "Flow-induced compaction of a deformable medium," Phys. Rev. E **93**, 023116 (2016).

[12] Jackson, G. W. and James, D. F., "The permeability of fibrous porous media," Can. J. Chem. Eng. **64**, 364–374 (1986).

[13] Kugge, C., Bellander, H., and Daicic, J., "Pressure filtration of cellulose fibres," J. Pulp Pap. Sci. **32**, 95–100 (2005).

[14] Landman, K. A. and White, L. R., "Solid/liquid separation of flocculated suspensions," Adv. Colloid Interface Sci. **51**, 175–246 (1994).

[15] Landman, K. A., Sirakoff, C., and White, L. R., "Dewatering of flocculated suspensions by pressure filtration," Phys. Fluids A: Fluid Dyn. **3**(6), 1495–1509 (1991).

[16] Landman, K. A., Stankovich, J. M., and White, L. R., "Measurement of the filtration diffusivity D(ϕ) of a flocculated suspension," AIChE J. **45**(9), 1875–1882 (1999).

[17] Landman, K. A., White, L. R., and Eberl, M., "Pressure filtration of flocculated suspensions," AIChE J. **41**(7), 1687–1700 (1995).

[18] Lentle, R. G., Janssen, P. W. M., and Hume, I. D., "The roles of filtration and expression in the processing of digesta with high solid phase content," Comp. Biochem. Physiol. Part A: Mol. Integr. Physiol. **154**(1), 1–9 (2009).

[19] Lindsay, J. D., *The Anisotropic Permeability of Paper: Theory, Measurements, and Analytical Tools* (The Institute of Paper Chemistry, Appleton Wisconsin, 1988).

[20] McKenzie, D., "The generation and compaction of partially molten rock," J. Petrol. **25**, 713–765 (1984).

[21] Northcott, K. A., Snape, I., Scales, P. J., and Stevens, G. W., "Contaminated water treatment in cold regions: An example of coagulation and dewatering modelling in antarctica," Cold Regions Sci. Technol. **41**(1), 61–72 (2005).

[22] Olivier, J., Vaxelaire, J., and Vorobiev, E., "Modelling of cake filtration: An overview," Sep. Sci. Technol. **42**(8), 1667–1700 (2007).

[23] Panshin, A. J. and de Zeeuw, C., *Textbook of Wood Technology*, 4th ed. (McGraw Hill, 1980).

[24] Paterson, D. T., "Understanding rapid dewatering of cellulose fibre suspensions," MASc thesis, Department of Mechanical Engineering, University of British Columbia, 2016.

[25] Pettersson, P., Wilkström, T., and Lundström, T. S., "Method for measuring permeability of pulp suspension at high basis weights," J. Pulp Pap. Sci. **34**, 191–197 (2008).

[26] Spiegelman, M., "Flow in deformable porous media. I. Simple analysis," J. Fluid Mech. **247**, 17–38 (1993).

[27] Stickland, A. D. and Buscall, R., "Whither compressional rheology?," J. Non-Newtonian Fluid Mech. **157**(3), 151–157 (2009).

[28] Vomhoff, H., *Dynamic Compressibility of Water-Saturated Fibre Networks and Influence of Local Stress Variations in Wet Pressing* (Department of Pulp and Paper Chemistry and Technology, Royal Institute of Technology, 1998).

[29] Vomhoff, H., "On the in-plane permeability of water-saturated fibre webs," Nord. Pulp Pap. Res. J. **15**(3), 200–210 (2000).

[30] Vomhoff, H. and Schmidt, A., "The steady-state compressibility of saturated fibre webs at low pressures," Nord. Pulp Pap. Res. J. **12**(41), (1997).

[31] Wakeman, R. J., "Separation technologies for sludge dewatering," J. Hazard. Mater. **144**(3), 614–619 (2007).